# From chimeras to extensive chaos in networks of heterogeneous Kuramoto oscillator populations

Pol Floriach,[1] Jordi Garcia-Ojalvo,[2] and Pau Clusella[3]

[1)]*ETSETB, Universitat Politècnica de Catalunya, Barcelona (Spain)*

[2)]*Department of Medicine and Life Sciences, Universitat Pompeu Fabra, Barcelona (Spain)*

[3)]*EPSEM, Departament de Matemàtiques, Universitat Politècnica de Catalunya, Manresa (Spain)*

(*Electronic mail: pau.clusella(at)upc.edu)

Networks of coupled oscillators can exhibit a wide range of complex dynamical behavior, from complete synchronization to chimera and chaotic states. Here we analyze the dynamics of networks of populations of heterogeneous mean-field coupled Kuramoto-Sakaguchi oscillators and show that the instability that leads to chimera states in a simple two-population model also leads to extensive chaos in large networks of coupled populations. Formally, the system consists of a complex network of interacting oscillator populations whose mesoscopic behavior evolves according to the Ott-Antonsen equations. By considering identical parameters across populations, the system contains a manifold of homogeneous solutions where all populations behave identically. Stability analysis of these homogeneous states provided by the Master Stability Function shows that non-trivial dynamics might emerge on a wide region of the parameter space for arbitrary network topologies. As examples, we first revisit the two-population case, and provide a complete bifurcation diagram. Then, we investigate the emergent dynamics in large ring and Erdös-Rényi networks. In both cases, transverse instabilities lead to extensive space-time chaos, i.e., irregular regimes whose complexity scales linearly with the system size. In summary, our work provides a unified analytical framework to understand the emergent dynamics of networks of Kuramoto populations, from chimera states to robust high-dimensional chaos.

## I. INTRODUCTION

Chimera states are an intriguing example of non-trivial collective activity emerging in networks of coupled oscillators. In their simple original form, chimera states consist of a population of identical oscillatory units spontaneously splitting into two subgroups: a completely synchronized cluster and a partially synchronized one[1,2]. This form of spontaneous symmetry breaking was first uncovered in non-locally coupled rings of phase oscillators, and has since been studied in a wide variety of theoretical and real systems[3,4].

The Kuramoto-Sakaguchi model[5] provides a simple yet powerful framework to understanding the collective behavior of complex oscillatory systems, including chimera states. In this model, each oscillator corresponds to a single phase variable which interacts with other units through all-to-all sinusoidal coupling. Remarkably, this mean-field setup allows an exact low-dimensional reduction through the Ott-Antonsen ansatz[6,7]. This method provides the collective dynamics of the system as a single differential equation for the complex Kuramoto order parameter[8].

Researchers have employed the Ott-Antonsen equations to unveil the nature of chimera states in systems composed of two identical populations of Kuramoto-Sakaguchi oscillators[2,9–12]. For oscillators with equal natural frequencies, the chimera state always coexist with the homogeneous solution (i.e., full synchronization of the two populations)[13]. However, for oscillators with distributed frequencies, the chimera state might emerge through a pitchfork bifurcation of the homogeneous solution, thus attracting solutions are always inhomogeneous in wide regions of the parameter space[9,11]. Interestingly, chimera states are not always stable in these regions, leading to the emergence of other regimes in-

cluding symmetric oscillations, antiphase states, or even low-dimensional chaos[9–12][14] .

A natural question to ask is how do these results transduce to large networks of more than two populations. A number of recent studies have addressed this topic[15–19] (see also [7] for a thorough review). In particular, Martens [15 and 16] studied networks of three populations without disorder, and unveiled the emergence of different types of chimera states. Lee and Krischer [17] extended these studies and showed the emergence of low-dimensional chaos in the three-population model. The same authors also investigated six populations on a ring topology, and showed that chimeras are generally unstable, but connected through attracting heteroclinic cycles[18]. On the other hand, Laing [19] investigated the emergence of chimera states in rings composed of different number of populations with non-local coupling. Interestingly, this work unveils chaotic dynamics appearing through the instability of chimera states, and shows that this irregular regime vanishes as the number of populations in the network increases.

In spite of all this progress, the behavior of identical populations Kuramoto-Sakaguchi populations interacting through complex networks remains an open problem due to the variety of possible topological configurations. In this paper, we take on this challenge, and provide a general unifying framework to study the emergence of spatiotemporal dynamics in these models. We consider networks where the overall external input to each population is normalized across nodes, ensuring thus the existence of homogeneous states. The stability of these trivial regimes to small perturbations can be studied by means of the Master Stability Function[20], which provides the growth rate of arbitrary perturbations as a function of the structural connectivity eigenmodes. This method allows to obtain an analytical expression for the dispersion relation of the trivial states.

We show that, for populations with intrinsic disorder, transverse instabilities of the homogeneous state arise in a wide region of the parameter space for arbitrary network topologies. In the two-population model, this transverse instability corresponds to the pitchfork bifurcation leading to chimera states[9,11], whereas in large networks of ring and Erdős-Rényi topologies, the dynamics becomes immediately chaotic with several positive Lyapunov exponents. Numerical simulations reveal this is a case of extensive chaos, a dynamical regime in which the dimension of the chaotic attractor increases linearly with the system size. Extensive chaos, first conjectured by Ruelle[21], has been widely studied in spatially extended systems (usually under the more general term of "space-time chaos")[22,23], networks of spiking neurons[24,25], and mean-field models[26] among other systems. Nonetheless, to the best of our knowledge, this phenomena had never been reported in networks of Kuramoto oscillators before.

Overall, our study presents a general analytical approach to study the dynamics of networks of identical Kuramoto-Sakaguchi populations, and provides a direct link between the emergence of chimera states in two populations and the appearance of extensive chaos in large networks.

## II. A NETWORK OF KURAMOTO-SAKAGUCHI OSCILLATOR POPULATIONS

Let us consider $N$ populations composed of $M$ Kuramoto-Sakaguchi oscillators each[5,7]. Each oscillator in a population is described by their phase variable $\phi_{j,\sigma}$ where $j = 1, \ldots, M$ and $\sigma \in 1, \ldots, N$. The phase dynamics are given by

$$\dot{\phi}_{j,\sigma} = \omega_{j,\sigma} + \frac{K}{M} \sum_{\kappa=1}^{N} c_{\sigma\kappa} \sum_{m=1}^{M} \sin\left(\phi_{m,\kappa} - \phi_{j,\sigma} - \alpha\right) \quad (1)$$

where $\omega_{j,\sigma}$ are the natural frequencies of each oscillator, $K$ is a global coupling strength parameter, and $\alpha$ is the Sakaguchi phase-shift parameter. In this equation, both the intra and inter-population couplings are set via a mean-field, i.e., if populations $\sigma$ and $\kappa$ are coupled, then all oscillators in both populations contribute identically to the interaction. Therefore the only source of irregularity in the interactions is set by the inter-population connectivity, which is determined by a weighted complex network with connectivity matrix $C = (c_{\sigma\kappa})$. We impose two constrains on this connectivity:

- We assume $C$ row-normalized, i.e., $\sum_{\kappa=1}^{N} c_{\sigma\kappa} = 1$, thus, the total influence received by each oscillator is the same across populations.

- We assume $C$ is diagonalizable. This condition is always fulfilled if the network is undirected.

Generally we focus in cases where the internal coupling within each population is larger than the coupling between other populations, i.e., $c_{\sigma\sigma} > c_{\sigma\kappa}$ for all $\sigma \neq \kappa$. Nonetheless, this is not a strict requirement.

The natural frequencies of the oscillators $\omega_{j,\sigma}$ are distributed according to a Cauchy (Lorenz) distribution centered at $\overline{\omega}$ and with half-width at half-maximum $\Delta$. Due to the rotational symmetry of the model, we can set $\overline{\omega} = \tan(\alpha)(K\cos(\alpha) - \Delta)$ without loss of generality (see Appendix C), a choice that will be justified in the next section.

The complex Kuramoto order parameter of each population reads

$$Z_\sigma = R_\sigma e^{i\Phi_\sigma} = \frac{1}{M} \sum_{m=1}^{M} e^{i\phi_{m,\sigma}} \,.$$

By considering now that $M \to \infty$, we can apply the Ott-Antonsen ansatz[6], to obtain the evolution of $Z_\sigma$:

$$\dot{Z}_\sigma = (-\Delta + i\overline{\omega})Z_\sigma + \frac{K}{2} \sum_{\kappa=1}^{N} c_{\sigma\kappa} \left(Z_\kappa e^{-i\alpha} - Z_\sigma^2 Z_\kappa^* e^{i\alpha}\right) \,. \tag{2}$$

This equation provides the mean-field dynamics of each population in the network, and its attractiveness for $\Delta > 0$ has been recently proven[27]. Therefore, Eq. (2) is going to be our main object of study in the rest of the article.

## III. ANALYSIS OF HOMOGENEOUS STATES AND THEIR STABILITY

In order to explore the dynamics of (2), first we study its homogeneous manifold, i.e., all the states in which the $N$ populations evolve with exactly the same dynamics. By imposing $Z_\sigma = Z \; \forall \sigma$, into Eq. (2) and exploiting the fact that $C$ is row-normalized, we obtain

$$\dot{Z} = (-\Delta + i\overline{\omega})Z + \frac{K}{2}\left(Ze^{-i\alpha} - Z^2 Z^* e^{i\alpha}\right) \,, \tag{3}$$

which corresponds to the mean-field equation for a single, isolated population of Kuramoto-Sakaguchi oscillators[6,7]. The dynamics of this system are well studied: if $K < K_c := \frac{2\Delta}{\cos(\alpha)}$ the system converges to the incoherent state $Z^{(0)} := 0$. At $K = K_c$ the system undergoes a supercritical Hopf bifurcation ($H_0$ in the figures) giving rise to a synchronized or coherent state $Z := Re^{i\Omega t}$ with

$$R = \sqrt{1 - \frac{2\Delta}{K\cos(\alpha)}} \tag{4}$$

$$\Omega = \overline{\omega} - \tan(\alpha)(K\cos(\alpha) - \Delta) \,.$$

These equations show that our choice of the mean frequency $\overline{\omega} = \tan(\alpha)(K\cos(\alpha) - \Delta)$ defines a co-rotating frame in which the homogeneous coherent solution is a steady state rather than a limit-cycle (i.e., $\Omega = 0$). This simplifies the following analytical calculations.

Next, we focus on the stability of the coherent homogeneous state $Z$ given by Eq. (4). The same analysis for the incoherent homogeneous solution $Z^{(0)}$ is provided in Appendix E, where we show that no instabilities occur below the Kuramoto

synchronization transition $H_0$. Let us consider a small perturbation of the coherent homogeneous state, $Z_\sigma = Z + z_\sigma$. Linearizing Eq. (2) we obtain

$$\dot{z}_\sigma = (-\Delta + i\overline{\omega} - KR^2 e^{i\alpha})z_\sigma$$
$$+ \frac{K}{2} \sum_{\kappa=1}^{M} c_{\sigma\kappa}(z_\kappa e^{-i\alpha} - R^2 z_\kappa^* e^{i\alpha}) . \quad (5)$$

In order to lighten notation, in the following steps we express complex quantities in a vectorial format: $z = (x, y)^T$ where $x$ and $y$ are the real and imaginary parts of $z$ respectively. Then, Eq. (5) can be expressed as

$$\dot{z}_\sigma = Az_\sigma + B \sum_{\kappa=1}^{M} c_{\sigma\kappa} z_\kappa \quad (6)$$

where

$$A = \begin{pmatrix} \Delta - K\cos(\alpha) & -\Delta\tan(\alpha) \\ \Delta\tan(\alpha) & \Delta - K\cos(\alpha) \end{pmatrix}$$

and

$$B = \begin{pmatrix} \Delta & \Delta\tan(\alpha) \\ -K\sin(\alpha) + \Delta\tan(\alpha) & K\cos(\alpha) - \Delta \end{pmatrix}$$

are obtained by inserting the values of $\overline{\omega}$ and $R$ derived from Eq. (4) into Eq. (5) and separating real and imaginary parts.

Next, we apply the Master Stability Formalism[20] in order to simplify the analysis of Eq. (6)[28]. This method consists on decomposing the perturbation $z_\sigma$ on the basis provided by the diagonalization of the connectivity matrix $C$. We denote the eigenvalues of the connectivity matrix as $\Lambda_1 \geq \Lambda_2 \geq \cdots \geq \Lambda_N$, and the corresponding eigenvectors as $\mathbf{\Psi}^{(k)} = (\Psi_1^{(k)}, \ldots, \Psi_N^{(k)})^T$ with $k = 1, \ldots, N$. Therefore

$$C\mathbf{\Psi}^{(k)} = \Lambda_k \mathbf{\Psi}^{(k)} . \quad (7)$$

Then, we express the perturbation $z_\sigma$ on the basis composed of $\mathbf{\Psi}_k$ for $k = 1, \ldots, N$ as

$$z_\sigma = \sum_{k=1}^{N} u_k \otimes \Psi_\sigma^{(k)} \quad (8)$$

where $u_k \in \mathbb{C}$ are the coordinates of $z_\sigma$ in the new basis and $\otimes$ is the Kronecker product.

Inserting Eq. (8) in the linearization provided by Eq. (5) and

making use of Eq. (7) we derive the following expression:

$$\dot{z}_\sigma = \sum_{k=1}^{N} \dot{u}_k \otimes \Psi_\sigma^{(k)}$$
$$= A\sum_{k=1}^{N} u_k \otimes \Psi_\sigma^{(k)} + B\sum_{\kappa=1}^{N} c_{\sigma\kappa} \sum_{k=1}^{N} u_k \otimes \Psi_\kappa^{(k)}$$
$$= \sum_{k=1}^{N} \left[ Au_k \otimes \Psi_\sigma^{(k)} + Bu_k \otimes \sum_{\kappa=1}^{N} c_{\sigma\kappa} \Psi_\kappa^{(k)} \right]$$
$$= \sum_{k=1}^{N} \left[ Au_k \otimes \Psi_\sigma^{(k)} + \Lambda_k Bu_k \otimes \Psi_\sigma^{(k)} \right]$$
$$= \sum_{k=1}^{N} \left[ A + \Lambda_k B \right] u_k \otimes \Psi_\sigma^{(k)} .$$

Then, since the eigenvectors $\mathbf{\Psi}^{(k)}$ compose a basis of $\mathbb{R}^N$, linear independence provides

$$\dot{u}_k = \left[ A + \Lambda_k B \right] u_k .$$

Therefore, we decomposed the $2N \times 2N$ linear system Eq. (6) into $N$ 2-dimensional linear systems that depend on the eigenvalues $\Lambda_k$.

The eigenvalues $\lambda_k^{(\pm)}$ of the matrices $A + \Lambda_k B$ for $k = 1, \ldots, N$ characterize the stability of the homogeneous solution (4). In fact, they correspond to the *Floquet exponents* of the periodic solution $Z = Re^{i\Omega t}$. The analytical expression for the eigenvalues reads:

$$\lambda_k^{(\pm)} = \Delta + K\cos(\alpha)\left(\frac{\Lambda_k}{2} - 1\right)$$
$$\pm \left\{ \frac{K^2 \Lambda_k^2 \cos^2(\alpha)}{4} \right.$$
$$+ K\Lambda_k \Delta \cos(\alpha)\left[\tan^2(\alpha)(1 - \Lambda_k) - \Lambda_k\right]$$
$$\left. + \Delta^2\left[(\Lambda_k^2 - 1)\tan^2(\alpha) + \Lambda_k^2\right]\right\}^{1/2} . \quad (9)$$

This corresponds to a dispersion relation analogous to that in reaction-diffusion systems, with the structural eigenmodes $\mathbf{\Psi}^{(k)}$ playing the role of wave functions.

The eigenvalues $\lambda_k^{(\pm)}$ depend explicitly on the parameters of the system ($\Delta$, $\alpha$, and $K$), as well as the structural eigenvalues $\Lambda_k$. Using the row-normalization of $C$ and the Gershgorin circle theorem[29] we can assert that $|\Lambda_k| \geq 1$. Moreover, the largest structural eigenvalue is $\Lambda_1 = 1$, and the corresponding eigenvector corresponds to a uniform perturbation, i.e.,

$$\mathbf{\Psi}^{(1)} = \frac{1}{\sqrt{N}}(1, \cdots, 1)^T.$$

From the expression of $\lambda_k$ in Eq.(9) we see that $\lambda_1^+ = 0$, as it should, since the homogeneous state is a limit-cycle in a co-rotating frame. The eigenvalues $\lambda_k$ for $k > 1$ indicate the

growth rates of perturbations that are transverse to the homogeneous manifold.

For the case $\Delta = 0$ the expression of the system eigenvalues simplify to $\lambda^{(+)} = K\cos(\alpha)(\Lambda - 1)$ and $\lambda^{(-)} = -K\cos(\alpha)$. Since the coherent state emerges for $K\cos(\alpha) > 2\Delta = 0$, this proves that, in networks without disorder, the homogeneous state is always stable, consistent with the fact that chimera states in these systems always coexist with the full synchronized solution[13].

For $\Delta > 0$, however, the scenario changes. In this case it is possible to perform parameter a reduction (see Appendix C), thus we set $\Delta = 1$ without loss of generality, and analyze the system for different values of $K$ and $\alpha$. Fig. 1(a) shows $\mathrm{Re}[\lambda^{(\pm)}]$ as a function of $\Lambda$ for different parameter sets. For the selected values, the dispersion relation displays a positive region, indicating the existence of transverse instabilities, which always emerge through real eigenvalues $\lambda^{(+)} \in \mathbb{R}$[30]. Overall, the shape of the dispersion relation resembles that of the Benjamin-Feir instability in the complex Ginzburg-Landau equation[31].

Setting $\mathrm{Re}[\lambda^{(+)}] = 0$ in Eq (9) determines the regions where transverse instabilities of the homogeneous state arise in the parameter space. Figure 1(b) shows such regions for three different values of $\alpha$ in the $(K, \Lambda)$-plane. A small region of instabilities arise already for $\alpha = 1$, and widens as $\alpha \to \pi/2$, the critical value at which the homogeneous coherent solution vanishes through $H_0$. This is consistent with previous findings showing that chimera and other symmetry-breaking states emerge only for $\alpha$ close but below $\pi/2$[2,11,13]. In the next sections we review the dynamics that emerge in this region in the two-population model, ring networks, and Erdős-Rényi connectivites. For this analysis we fix $\alpha = 1.2$, a value not that close to the $H_0$ bifurcation, and still displaying a large instability region.

## IV. REVIEW OF THE TWO-POPULATION MODEL

As a first example we revisit the two-population model. Previous works on this setup showed the emergence of chimera and other states from a pitchfork bifurcation of the homogeneous synchronized state if $\Delta > 0$[9–12]. Here we show that such bifurcation corresponds to a transverse instability provided by Eq. (9), and review some of the dynamics emerging from this symmetry-breaking. In order to simplify the analysis, we fix $\Delta = 1$ without loss of generality (see Appendix C). This choice is purposely different from that used in previous studies in order to highlight that "weak heterogeneity" is not a requirement for the emergence of this rich bifurcation scenario. Similarly, we fix $\alpha = 1.2$, a value relatively far from the synchronization transition at $\alpha = \pi/2$.

The connectivity matrix in the 2-population model reads

$$C = \begin{pmatrix} \mu & 1 - \mu \\ 1 - \mu & \mu \end{pmatrix} . \tag{10}$$

where $\mu \in [0, 1]$ is a parameter controlling the coupling strength within the population, and $1 - \mu$ corresponds to the
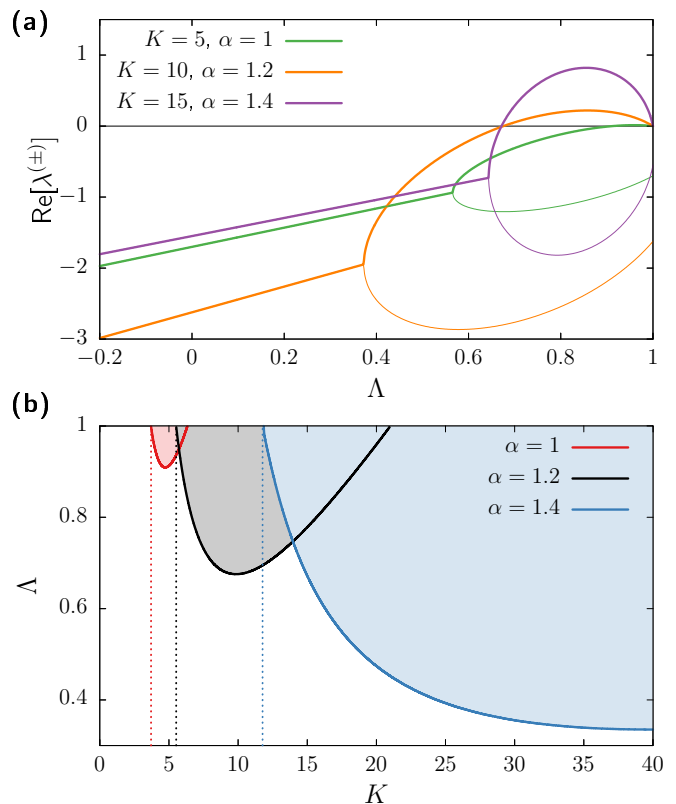


FIG. 1. Transverse instabilities of homogeneous states in networks of Kuramoto-Sakaguchi populations Eq. (2). (a) Real part of the eigenvalues characterizing the stability of the homogeneous solution $\lambda^{(\pm)}$ as a function of the structural matrix eigenvalues $\Lambda$. Thick and thin curves correspond to $\lambda^{(+)}$ and $\lambda^{(-)}$ as given by the Master Stability Function in Eq. (9) respectively. Green, orange, and purple curves correspond to $(K, \alpha) = (5, 1)$, $(10, 1.2)$, and $(15, 1.4)$. (b) Color-shaded regions show the regions of transverse instability in the $(K, \Lambda)$ plane, with solid lines showing the loci of the bifurcation ($\mathrm{Re}[\lambda^{(+)}] = 0$ in Eq. (9)). Dotted vertical lines indicate the Kuramoto synchronization transition $K_c = 2\Delta / \cos(\alpha)$ at which the coherent homogeneous solution emerges. Results shown for $\alpha = 1$ (red), 1.2 (black), and 1.4 (blue).

coupling strength across the two populations.

The eigenvalues of this connectivity matrix read $\Lambda_1 = 1$ and $\Lambda_2 = 2\mu - 1$. Substituting $\Lambda_2$ in Eq. (9) and setting $\mathrm{Re}[\lambda_2^{(+)}] = 0$ provides an analytical expression for the pitchfork bifurcation of the homogeneous state as an implicit equation on the system parameters. Black curve in Figure 2(a) shows such bifurcation line in the $(K, \mu)$-plane, with the color-shaded region indicating the region of instability (see also black curve in 1(b)). Within this region, four different states might exist (apart from the incoherent and coherent homogeneous states)[33]:

- **Steady chimera**, a fixed point characterized by $R_1 \neq R_2$.

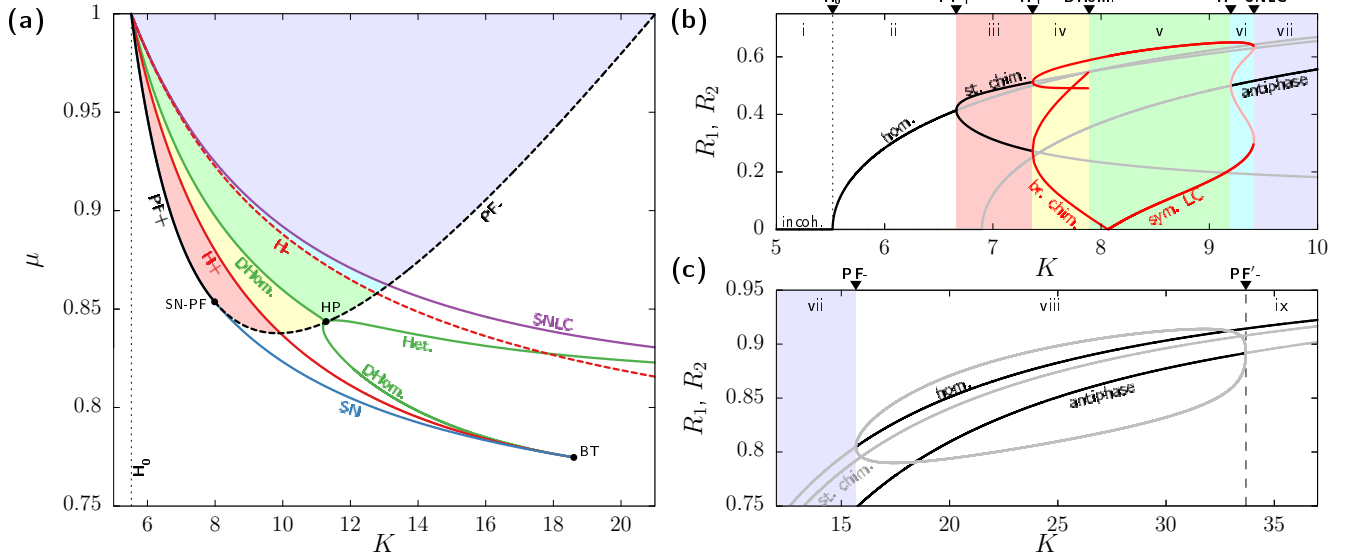- **Breathing chimera**, a limit-cycle characterized by one population having always a larger degree of synchrony

FIG. 2. Bifurcation diagrams of the two population model (Eq. (2) with Eq.(10)) for $\alpha = 1.2$ and $\Delta = 1$. (a) Two-parameter bifurcation diagram. Solid lines indicate supercritical bifurcations (+) and dashed lines indicate subcritical bifurcations (-). Black curves correspond to the pitchfork bifurcation (PF) of the homogeneous state (given by Eq. (9)), red curves indicate Hopf bifurcations (H), green curves indicate double homoclinic (DHom.) and heteroclinic (Het.) bifurcations, the blue curve indicates a saddle-node bifurcation (SN), and the purple curve indicates a saddle-node of limit-cycles (SNLC). Straight dotted thin line indicates the Kuramoto synchronization transition ($H_0$). Color-shaded regions indicate instability of the homogeneous solution, with each color corresponding to a different attractor set: red for stable steady chimeras, yellow for breathing chimeras, green for symmetric oscillations, blue for bistability between symmetric oscillations and antiphase state, and purple for stability of the antiphase fixed point only. (b,c) One-parameter bifurcation diagram for $\mu = 0.9$. Solid curves with different colors indicate different attractor types: Black for stable fixed points, grey for unstable fixed points, red for stable limit-cycles, and light red for unstable limit-cycles. Relevant bifurcations are labelled on the top of the figures, with the different regions between bifurcations shaded with the same color scheme as in panel (a). Most of these curves have been obtained with auto-07p[32] (see Appendix B).

than the other, i.e., either $R_1(t) > R_2(t)$ or $R_2(t) > R_1(t)$ for all $t > 0$ (see Fig. 3(a)).

- **Symmetric limit-cycle**, characterized by $R_1(t) = R_2(t + T/2)$, where $T$ is the period of the oscillation (see Fig. 3(b)).

- **Antiphase fixed point**, characterized by $R_1(t) = R_2(t)$ but $\Phi_1 - \Phi_2 = \pi$. A thorough analysis of this state, including linear stability, is provided in Appendix D.

In order to illustrate the emergence and nature of these different states, we first fix $\mu = 0.9$ and study the system dynamics upon increasing $K$ with the help of numerical continuation software[32]. The resulting bifurcation diagram is depicted in Figs 2(b) and (c) and can be split in nine different regions (labelled i-ix) delimited by different bifurcations:

(i) For $K < K_c \approx 5.52$ the incoherent state $Z_\sigma = Z^{(0)} = 0$ is the only stable solution. This state loses stability at the Kuramoto synchronization transition $H_0$, leading to the emergence of the coherent homogeneous state.

(ii) The coherent homogeneous state is the global attractor of the system from $H_0$ up to $K \approx 6.66$, when it loses stability through the supercritical pitchfork bifurcation (PF+) given by Eq. (9).

(iii) From PF+, two stable fixed points emerge, corresponding to steady chimeras (black lines in Fig. 2(b), red-shaded region). Although the steady chimeras coexist with the unstable homogeneous and antiphase fixed points, they are the sole attractor in this region of the parameter space.

(iv) At $K \approx 7.37$ the steady chimeras undergo a supercritical Hopf bifurcation (H+) leading to the emergence of two stable limit-cycles, corresponding to the breathing chimera (red lines in Fig. 2(b), yellow-shaded region). Fig. 3(a) shows exemplary time series of this state, and Fig.3(c) the corresponding phase portrait, with black curves depicting the limit-cycles and the red curve showing an example of a trajectory.

(v) The breathing chimera limit-cycles eventually collide with the unstable coherent homogeneous state at $K \approx 7.89$, merging in a single limit-cycle through a double homoclinic bifurcation (Dhom., also known as *gluing bifurcation*[10,34,35]). The resulting attractor corresponds to a symmetric limit cycle in which the two populations alternate the same level of synchrony half a period apart (red lines in Fig. 2(b), green-shaded region). Figure 3(b) shows exemplary time series of this regime and Figs. 3(d) and (e) depict two phase portraits, with $K$ in panel (d) very close to the gluing bifurcation.

(vi) At $K \approx 9.19$, the antiphase state of the system, which is unstable for smaller values of $K$, becomes stable through a subcritical Hopf bifurcation (H-, see Appendix D). Therefore, in this region of the bifurcation diagram there is bistability between the antiphase state and the symmetric limit-cycle (black and red lines in Fig. 2(b), blue-shaded region). Figure 3(f) shows the phase portrait of this bistable regime, with the unstable limit-cycle represented by a grey curve.

(vii) The symmetric limit-cycle collides with the unstable limit-cycle at $K \approx 9.41$, thus both solutions vanish through a saddle-node of limit-cycles (SNLC). Then, the antiphase state becomes the only attractor for a wide region of the parameter space (black curve in Figs. 2(b,c), purple-shaded region).

(viii) At $K \approx 15.67$ the homogeneous fixed point recovers stability through the (subcritical) pitchfork bifurcation provided by Eq. (9) (see PF- in Fig. 2(c)). Therefore, in this region both homogeneous and antiphase states share stability (black curves in Fig. 2(c)).

(ix) Finally, the unstable fixed points emerging from PF- collide with the antiphase solution at a new subcritical pitchfork bifurcation (PF'-) at $K \approx 33.69$ (see Appendix D for an analytical derivation of PF'-). From this point, further increase of $K$ does not lead to any other bifurcation, and the homogeneous state remains the only (global) attractor of the system (black curve in Fig. 2(c)).

The two-parameter bifurcation diagram in Fig. 2(a) shows that the bifurcation scenario we have described for $\mu = 0.9$ holds for the entire region of instability of the homogeneous state. The diagram also shows the loci of a saddle node bifurcation (SN) that joints the pitchfork bifurcation (PF) at a fold-pitchfork codimension-2 bifurcation (SN-PF). At this codimension 2 point, the symmetry breaking bifurcation turns from supercritical to subcritical[9,11]. This SN branch limits a region of bistability between the homogeneous fixed point and stable chimeras. Within this region, following a route similar to the one described before, the stable chimera turns to a breathing state at the supercritical Hopf (H+). Nonetheless, in this case the gluing bifurcation leads to the disappearance of limit-cycle solutions, since the homogeneous state is stable. Finally, there is an additional region of bistability between the asymmetric limit cycle and the homogeneous state bounded by a heteroclinic bifurcation and the saddle-node of limit cycles (SNLC).

Altogether, this analysis unveils a rich dynamical landscape emerging from the pitchfork bifurcation breaking the symmetry of the homogeneous state. These results complement those presented in previous works for the same system[9–12] but without relying on weak heterogeneity. Morevoer, the pitchfork bifurcation of the homogeneous state (PF) and the bifurcations from the antiphase state (H- and PF'-) have been obtain analytically as an implicit equation on the system parameters.

## V. RING TOPOLOGY

Now we consider a ring network composed of $N > 2$ populations connected via nearest neighbors. The connectivity matrix $C = (c_{\sigma\kappa})$ reads

$$
c_{\sigma\kappa} = \begin{cases} \mu & \text{if} \quad \sigma = \kappa \\ \frac{1-\mu}{2} & \text{if} \quad |\sigma - \kappa| = 1 \text{ or } N - 1 \\ 0 & \text{otherwise} . \end{cases} \tag{11}
$$

This scenario was studied in Ref. [18] for the case of $N = 6$ oscillators, where they unveiled different forms of stable and (non-chaotic) breathing chimera for heterogeneous populations. Also, Ref. [19] analyzed a similar ring model but with non-local coupling, which displayed chaotic solutions that vanish upon increasing system size. Here we show that, in our setup, transverse instabilities of the homogeneous state lead to chaotic dynamics that show an extensive character with $N$, i.e., the dynamical complexity of the system scales linearly with the system size.

Since $C$ is a circulant matrix, its eigenvalues have a simple expression. In order to preserve the ordering from larger to smaller, we write them as

$$
\Lambda_k = \begin{cases} \mu + (1 - \mu) \cos \left( \frac{\pi}{N}(k - 1) \right) & \text{if } k \text{ is odd,} \\ \mu + (1 - \mu) \cos \left( \frac{\pi}{N}k \right) & \text{if } k \text{ is even,} \end{cases} \tag{12}
$$

for $k = 1, \ldots, N$. The corresponding eigenvectors are the discrete Fourier modes

$$
\Psi_j^{(k)} = \begin{cases} \dfrac{e^{\frac{\pi j}{N}(k-1)i}}{\sqrt{N}} & \text{if } k \text{ is odd,} \\ \dfrac{e^{-\frac{\pi j}{N}ki}}{\sqrt{N}} & \text{if } k \text{ is even,} \end{cases} \tag{13}
$$

where $k = 1, \ldots, N$.

As $N$ increases, the second largest structural eigenvalue $\Lambda_2$ tends to 1. Therefore, from Fig. 1(b), we infer that the region of transverse instability expands with $N$. Fig. 4(a) illustrates this situation: Thick continuous curves depict the bifurcation obtained from setting $\text{Re}[\lambda^{(+)}] = 0$ in Eq. (9) in the $(K, \mu)$-plane. As $N$ increases, the region of instability becomes larger, covering a wide band of $K$ values irrespective of $\mu$ if $N$ is sufficiently large. Moreover, the emergence of instabilities occurs arbitrarily close to the Kuramoto synchronization transition ($H_0$, vertical black dashed line in Fig. 4(a)).

Another important aspect of the ring spectrum in Eq. (12) is that it is delocalized, i.e., it covers the interval $\Lambda_k \in [2\mu - 1, 1]$ densely as $N \to \infty$. Therefore, several structural eigenmodes $\Lambda_k$ might correspond to unstable directions concurrently. For instance, the colored region in Fig. 4(b) shows the number of unstable directions of the homogeneous state in the $(K, \mu)$-plane for $N = 128$. The number of positive growth rates generally increases with $\mu$, with a large region (dark blue) where all $\lambda_k^{(+)} > 0$ for $k > 1$. In fact, this region coincides with the region of transverse instability for the two-population
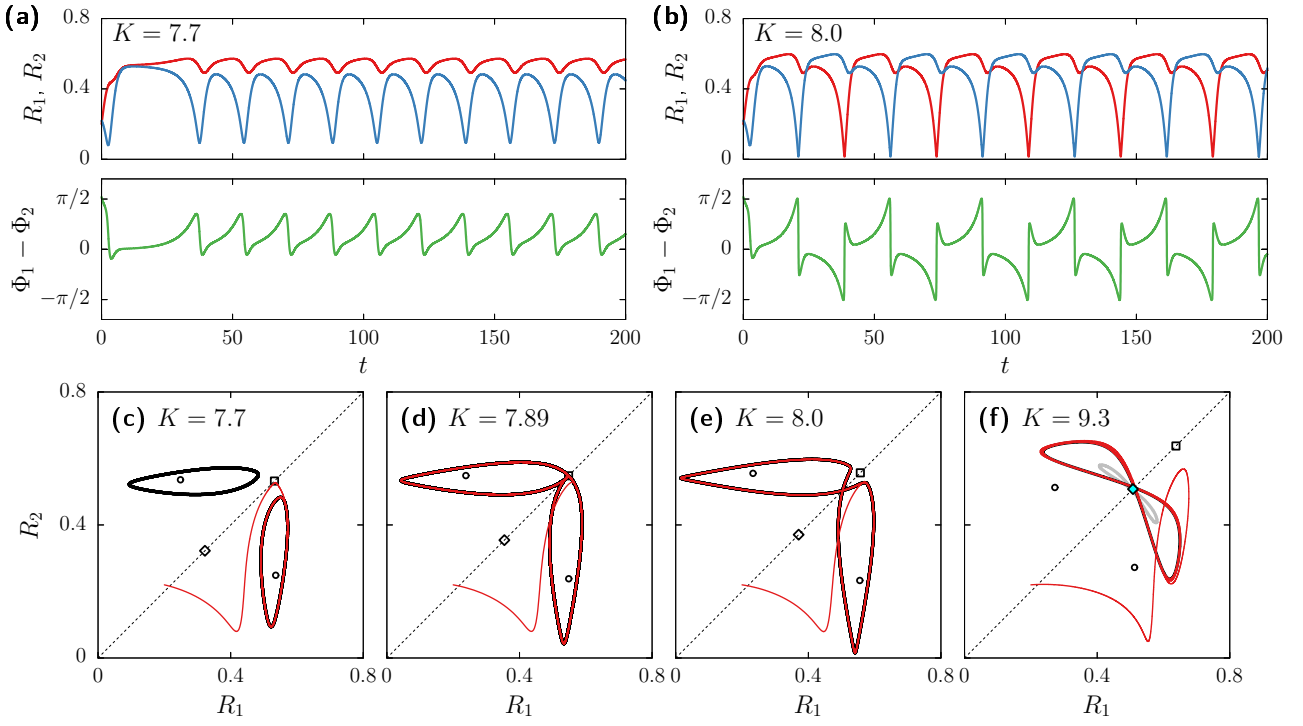
FIG. 3. Oscillatory dynamics in the 2-population Kuramoto model (Eq. (2) with Eq. (10)) for $\mu = 0.9$, $\alpha = 1.2$, and $\Delta = 1$. (a,b) Time series of the Kuramoto order parameters and phase difference of the two populations at a breathing chimera state (panel (a), $K = 7.7$) and asymmetric limit-cycle (panel (c), $K = 8$). (c-f) Phase portraits for different values of $K$ showing breathing chimera (panel (c)), the symmetric limit-cycle (panels (d) and (e)), and bistability between the antiphase state and the symmetric limit-cycle (panel (f)). Bold black curves show the stable limit-cycles and red curves show an exemplary trajectory. Grey curven in panel (f) shows the unstable limit-cycle. Open symbols correspond to the different unstable fixed points: square ($\square$) indicates the homogeneous state, diamond ($\diamond$) indicates the antiphase state, circles ($\circ$) indicate the two steady chimera states. Blue-colored diamond in panel (f) indicates the stable antiphase state.

model, since the last mode turning unstable corresponds to $\Lambda_N = 2\mu - 1$.

The regularity of ring topologies also allows for the existence of antiphase and other twisted states[18]. Appendix D provides a linear stability analysis for antiphase states in ring networks. Thin lines in Fig. 4(a) and red curve in (b) delimit the region of stable antiphase dynamics. This region shrinks by increasing $N$, although the changes are less prominent than those of the homogeneous state (see Appendix D for a further discussion).

Overall, in large ring networks, we expect to have complex dynamics in wide regions of the parameter space due to the expansion of the transverse instability region and the number of unstable directions of the homogeneous state. Figure 5 shows two instances of these complex dynamics for $N = 128$. Pannels (a) depict $R_\sigma$ and $\Phi_\sigma$ of each population over time for parameters in the region where the number of unstable directions of the homogeneous state is maximal ($K = 7$, $\mu = 0.9$). The dynamics of $R_\sigma$ are rather hectic, with $\phi_\sigma$ showing some indications of spatial structure. Instead, panels (b) correspond to parameters associated with less unstable directions ($K = 15$, $\mu = 0.5$). In this case, the dynamics of both $R_\sigma$ and $\Phi_\sigma$ evolve more regularily in spite of their seemingly chaotic behavior. These qualitative observations posit the existence of space-time chaos emerging from the transverse instabilities. In the

rest of this section, we asses the chaotic and complex behavior of the system by means of numerical Lyapunov analysis. Appendix A contains precise definitions of the monitored quantities.

First, we focus on a fixed network size ($N = 128$) and study the dynamics by varying $K$. Figures 6(a1-d1) show the numerical results obtained with fixed $\mu = 0.9$, thus covering the region of maximal number of unstabilities. Red circles in Figure 6(a1) show the time average of the network's mean Kuramoto order parameter, $\mathcal{R}$. The shaded region shows the corresponding standard deviation $\mathcal{S}$ (see Appendix A for specific definitions). Grey continuous lines indicate the value of $\mathcal{R}$ corresponding to the homogeneous and antiphase states (Eqs. (4) and (D1)). As predicted, the nontrivial dynamics emerge just after the Kuramoto transition to synchrony $H_0$ and appear to be the only attracting state until the stabilization of the antiphase state (see dotted vertical lines).

To characterize the complexity of these non-trivial states, Fig. 6(b1) displays the 20 largest Lyapunov exponents $\ell_\sigma$ of the network. At the transverse instability, many exponents become positive at once, thus indicating the emergence of high-dimensional chaotic dynamics. Indeed, the Kaplan-Yorke formula (Fig. 6(c1)) indicates a fractal dimension with about $\mathcal{D}_{KY} \approx 28$ degrees of freedom just after the transition. The attractor dimension increases smoothly until it
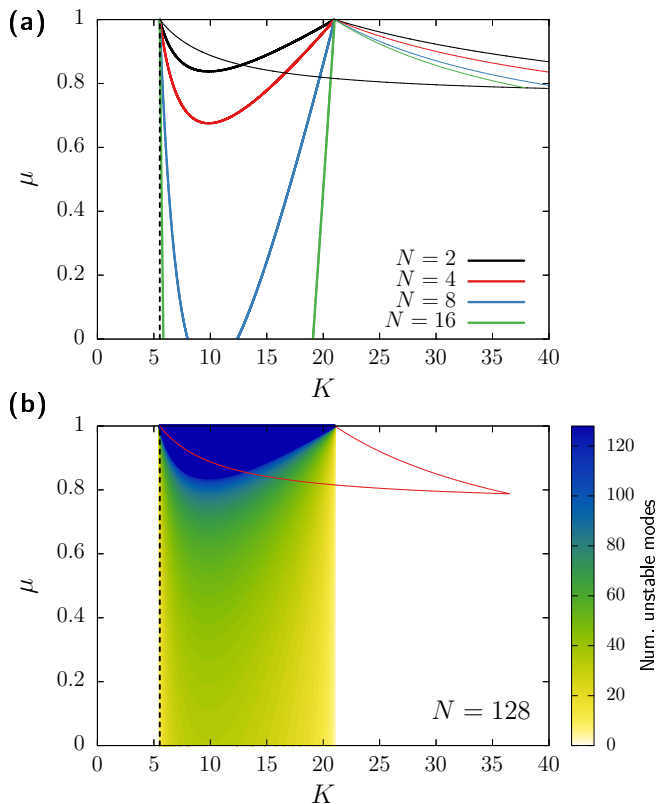
FIG. 4. Transverse instabilities of the homogeneous and antiphase state in ring networks ($\alpha = 1.2$ and $\Delta = 1$). (a) Thick lines indicate the region of transverse instability of the homogeneous state for different $N$. Thin curves indicate the region of stability of the antiphase state. (b) Color-shaded regions show the number of unstable modes of the homogeneous state for a network of $N = 128$ populations. Red curve indicates the corresponding region of stability of the antiphase state. Vertical black dashed line indicates the Kuramoto synchronization ($H_0$) transition in both panels.

reaches a maximum of $\mathcal{D}_{KY} \approx 200$, and then slowly decreases until vanishing at the stabilization of the antiphase state. Similarly, the Kolmogorov-Sinai dynamical entropy $h_{KS}$ (Fig. 6(d1)) also increases starting at the transverse instability, albeit it does so less abruptly. This measure indicates that the maximum complexity of the trajectories is reached around $K \approx 7.5$. Altogether, these results establish the existence of high-dimensional chaos arising from the transverse instabilities of the homogeneous state for $\mu = 0.9$.

Next, we switch to $\mu = 0.5$, for which the homogeneous state has less unstable directions. Moreover, the antiphase state does not exist for this value of $\mu$, and therefore, we expect non-trivial dynamics for a larger $K$-range. Figures 6(a2-d2) show that the scenario starts off analogously to that of $\mu = 0.9$: at the transverse instability (see vertical dotted line) the system transitions from incoherence to a state with a large degree of heterogeneity. Also, several Lyapunov exponents become positive at once, resulting into both $\mathcal{D}_{KY}$ and $h_{KS}$ increasing rapidly. Again, this corresponds to a case of space-time chaos. Nonetheless, around $K \approx 15.8$ a transition occurs

in which the irregularity of the system drops drastically.

The dynamics emerging from this bifurcation, which is not detected by our theory, evolve very close to the homogeneous state. In fact, our measure of network heterogeneity $\mathcal{S}$ does not capture spatial inhomogeneities (see red symbols in Fig.6(a2)). Nonetheless, a close inspection (not shown) revealed irregular space-time patterns in both, $R_\sigma$ and $\Phi_\sigma$, but the dynamics remains very close to the homogeneous solution and evolve rather slowly compared to the previous chaotic regime. The most clear indication of irregularity are the larger Lyapunov exponents, which are closer to zero, but many of them are still positive according to our numerics (see panels (b2-d2) in Fig.6). Finally, as shown by $\mathcal{D}_{KY}$, the dynamics fall back to the homogeneous state slightly after the predicted transition ($K \approx 21$, vertical dashed line in 6). This small offset between our analysis and the numerics is due to the slow convergence of small negative Lyapunov exponents in this regime.

So far, the numerical exploration for $\mu = 0.9$ and $\mu = 0.5$ proved the existence of highly complex spatiotemporal regimes emerging from transverse instabilities of the homogeneous state in rings of $N = 128$ populations. Next, we test the robustness and scaling these results upon varying the system size $N$. Fig. 7 shows results from simulations of rings composed of $N = 64, 128, 256, 512$ and $1024$ populations (red and blue symbols) for selected parameter values. Panel (a) shows the Lyapunov spectra computed for different system sizes with normalized node index. For the tested parameter values $((K, \mu) = (7, 0.9)$ and $(15, 0.5))$ the spectra shows a good collapse upon increasing $N$, with the only exception of the smaller networks for the second set (blue dots). This robust spectra upon increasing $N$ indicates extensive chaos, i.e., a chaotic regime with complexity scaling linearly with the system size. To further explore this possibility, Figs. 7(b) and (c) show the computed fractal dimension and dynamical entropy for the same parameter values upon increasing $N$. In all cases, an accurate scaling $\mathcal{D}_{KY} \propto N$ and $h_{KS} \propto$ is observed.

Overall, these numerical results indicate that transverse instabilities of a homogeneous state lead to extensive chaos in ring networks of oscillator populations with nearest neighbour coupling. In the next section we investigate the case of irregular topologies.

## VI. ERDŐS-RÉNYI NETWORKS

Here we discuss the dynamics that emerge in irregular network topologies. In order to simplify the analysis, we restrict ourselves on connectivities derived from Erdős-Rényi networks with fixed average degree $\bar{d} = 10$. Let $A = (a_{\sigma\kappa})$ be the adjacency matrix of an (undirected) Erdős-Rényi network (i.e., $a_{\sigma\kappa} \in \{1, 0\}$). Then, we consider a connectivity matrix $C = (c_{\sigma\kappa})$ given by

$$c_{\sigma\kappa} = \begin{cases} \mu & \text{if} \quad \sigma = \kappa \\ \dfrac{1-\mu}{d_\sigma} a_{\sigma\kappa} & \text{if} \quad \sigma \neq \kappa. \end{cases}$$
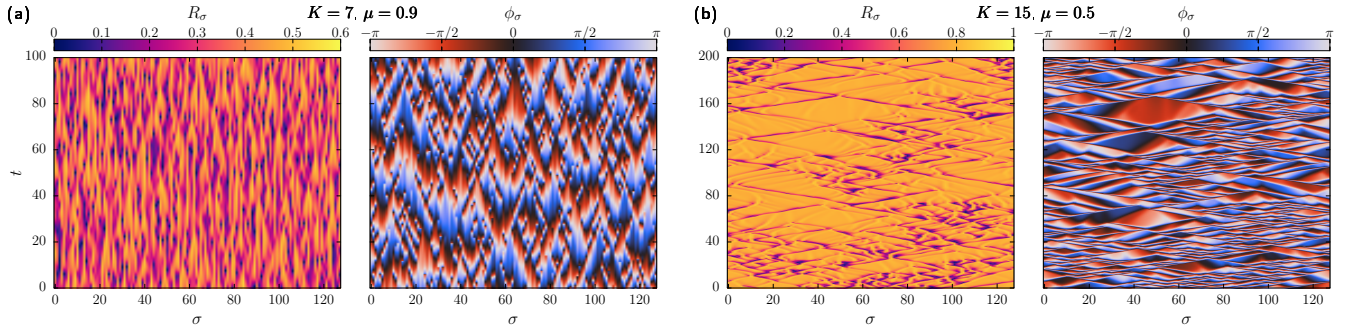
FIG. 5. Chaotic dynamics of the ring model for different parameter values ($\alpha = 1.2$ and $\Delta = 1$). (a) Kuramoto order parameter of each population $R_\sigma$ and corresponding phase $\Phi_\sigma$ for $K = 7$ and $\mu = 0.9$ after a transient of 1000 time units. (b) Same quantities for $K = 15$ and $\mu = 0.5$.
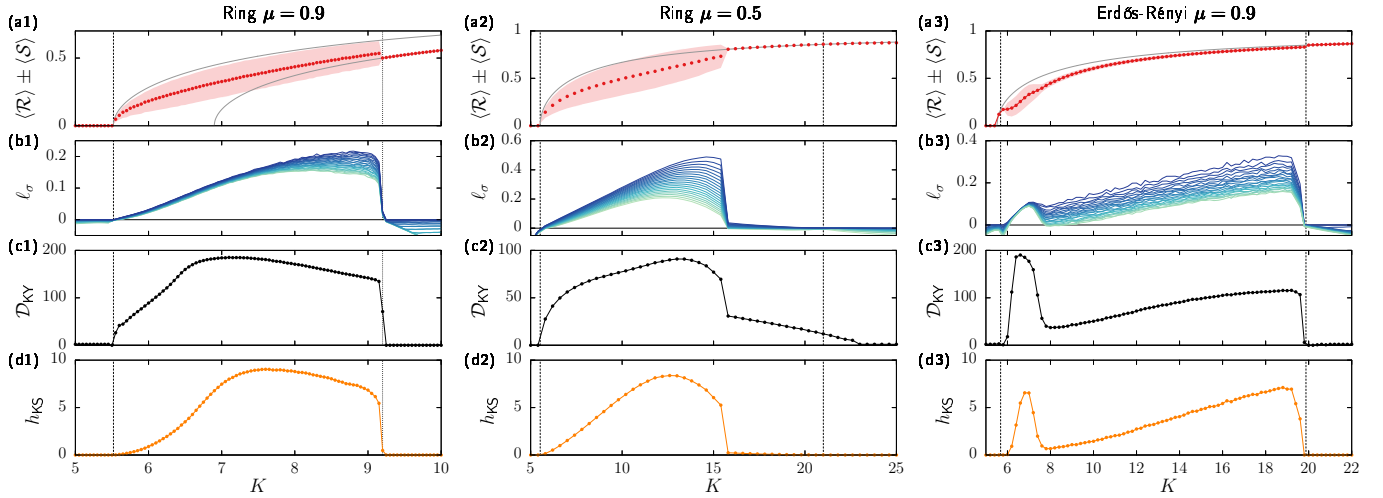


FIG. 6. Simulations of ring (columns 1 and 2) and Erdős-Rényi (column 3) networks with $N = 128$ ($\alpha = 1.2$ and $\Delta = 1$). (a) Red circles indicate time average mean activity $\langle \mathcal{R} \rangle$, with the red-shaded region showing the corresponding level of heterogeneity $\langle \mathcal{R} \rangle \pm \langle \mathcal{S} \rangle$. Grey curves correspond to the value of $R$ for the homogeneous states given by Eq. (4). In panel (a1) an additional grey curve shows the antiphase state (Eq. (D1)). (b) 20 largest Lyapunov exponents $\ell_\sigma$. (c) Kaplan-Yorke fractal dimension computed using the (complete) Lyapunov spectra as given by Eq. (A1). (d) Kolmogorov-Sinai dynamical entropy computed from Eq. (A2). In all panels, vertical dashed lines indicate the emergence of transverse instabilities as given by Eq. (9). Dotted vertical line in panels (a1-d1) indicates the emergence of stable antiphase state as given by Eq. (D2).

where $d_\sigma$ is the degree of node $\sigma$ in the Erdős-Rényi model. This connectivity preserves the row-normalization required for the existence of homogeneous states, as well as introduces the self-coupling strength parameter $\mu$.

Unlike the ring scenario, we are unaware of explicit analytical results on the spectra of $C$ (which does not need to coincide with the spectra of the adjacency matrix $A$). However, combining analytical arguments with a numerical exploration, we can provide an accurate estimation of the region of transverse instabilities. By the Gershgoring circle theorem[29], the eigenvalues of $C$ are contained in the interval $\Lambda_k \in [1, 2\mu-1]$. Therefore, based on Fig. 1(b), transverse instabilities of the homogeneous state will occur. The shape of the region will depend on the second largest eigenvalue $\Lambda_2$. If $\tilde{\Lambda}$ is an eigenvalue of the matrix $D^{-1}A = (a_{\sigma\kappa}/d_\sigma)$, then $\Lambda = \mu + (1-\mu)\tilde{\Lambda}$ is an eigenvalue of $C$. Averages over 100 simulated networks with different sizes show that $\tilde{\Lambda}$ are densely distributed in the

interval [-0.6,0.6]. In particular, $\tilde{\Lambda}_2 \approx 0.6$ as $N$ increases, and therefore $\Lambda_2 \approx 0.4\mu + 0.6$. Using this approximation in the MSF Eq. (9) provides the region of transverse instabilities for ER networks in the $(K, \mu)$ parameter space. Black region in Fig. 8 shows the region where at least one mode of the homogeneous state is unstable. Also in this case the number of unstable directions in the region increases with $N$, with the purple region in Fig. 8 indicating the parameter values for which the homogeneous state has a maximum number of unstable modes ($N - 1$).

In order to capture the emergent dynamics, Figure 6(a3-d3) displays the results of simulations performed with fixed $\mu = 0.9$ and different values of $K$ for an ER network of $N = 128$ populations. As in the ring networks, the numerical outcome shows a scenario of consistent high-dimensional chaos for most of the transverse instability region (indicated by vertical dashed lines). Interestingly, two different types of
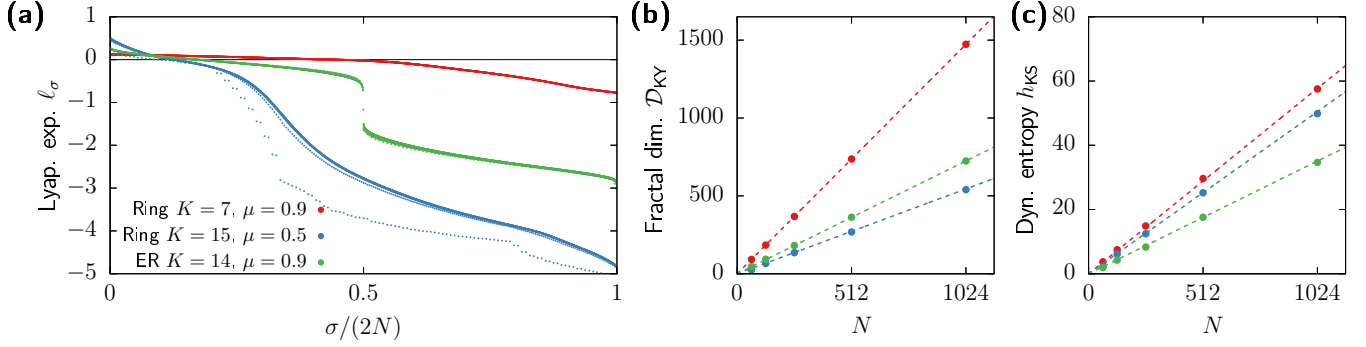
FIG. 7. Extensivity of chaos in ring and Erdős-Rényi (ER) networks ($\alpha = 1.2$ and $\Delta = 1$). (a) Complete Lyapunov spectra for different network sizes for the simulations of the ring and ER networks. For each parameter set, dots indicate the results for networks with $N = 64, 128, 256, 512$ and $1024$ populations. Nonetheless, in most cases differences across system sizes are barely visible. (b,c) Fractal dimension $D_{\mathbf{KY}}$ (panel b) and dynamical entropy (panel c) $h_{\mathbf{KS}}$ computed for different system sizes $N$ in three different simulation setups. Circles correspond to numerical simulations. Dashed lines correspond to a linear regression. In all these plots, red corresponds to ring networks with $K = 7$ and $\mu = 0.9$, blue corresponds to ring networks with $K = 15$ and $\mu = 0.5$, and green corresponds to ER networks with $K = 14$ and $\mu = 0.9$.
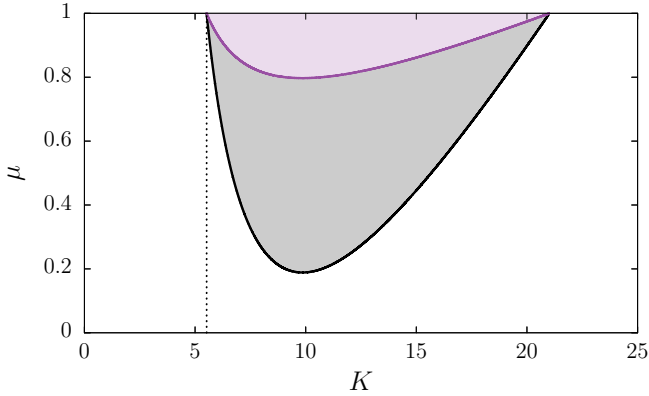


FIG. 8. Approximated region of transverse instabilities of the homogeneous state in Erdős-Rényi networks with average degree $\bar{d} = 10$. Black-shaded region indicates where at least one mode is unstable (i.e., $\mathrm{Re}[\lambda_2^{(+)}] > 0$). Purple-shaded region indicates where $N - 1$ modes are unstable. Vertical dashed line indicates the Kuramoto synchronization transition $\mathrm{H}_0$.

complex dynamics seem to emerge: First, the level of heterogeneity captured by $\mathcal{S}$ shows a region of high dynamical variety among nodes (see red-shaded region in panel (a3), $6 \lesssim K \lesssim 8$). In this case the Lyapunov spectra shows many exponents with similar positive values (panel (b3)), transducing to a very high Kaplan-Yorke dimension (panel (c3)) and dynamical entropy (panel (d4)). At $K \approx 8$, all measures show a significant reduction of complexity, indicating a transition to a different chaotic regime from $8 \lesssim K \lesssim 20$. In this case, the patterns lose heterogeneity, but the Lyapunov spectra still shows a regime of high-dimensional chaos. In fact, the number and value of the largest exponents increase monotonically with $K$, leading to an equally gradual increase of $\mathcal{D}_{\mathbf{KY}}$ and $h_{\mathbf{KS}}$ up to the stabilization of the homogeneous state ($K \approx 20$).

As in the ring model, we test the robustness of the chaotic

dynamics upon increasing network size. Green dots in Figure 7(a) show the entire Lyapunov spectra for $K = 15$ and $\mu = 0.9$ upon increasing system size. Apart from some deviations for the smaller network ($N = 64$), the different spectra show a good collapse. Moreover, green symbols in Fig.7(b) and (c) indicate that both fractal dimension and dynamical entropy increase linearly with $N$, confirming thus the extensive nature of the chaotic regime in ER topologies.

## VII. CONCLUSIONS

Recent works have studied the dynamics of networks of identical Kuramoto-Sakaguchi populations by means of the Ott-Antonsen equations under differerent parameter setups, coupling schemes, and system sizes[7,9,10,13,15–18,36]. This paper provides a leap forward in these efforts by providing a general expression for the instabilities of the homogeneous state as a function of the connectivity eigenmodes. We proved that, in networks without disorder ($\Delta = 0$), the homogeneous state is always transversally stable regardless the topology. On the other hand, for disordered populations ($\Delta > 0$), transverse instabilities occur. These instabilities, which lead to chimera states in two-population networks[9,11,12], give rise to extensive chaos in large nearest-neighbour ring and random connectivity schemes.

The emergence of extensive chaos in ring networks could apparently conflict with the findings of Laing[19], which studied a similar setup but with non-local connectivity via a discrete kernel. In their work, the row-normalization of the connectivity matrix is preserved, thus our theoretical framework also applies. The eigenvalues of their connectivity matrix can be analytically computed, and we found they are all zero except for three: $\Lambda_1 = 1$, $\Lambda_2 = \Lambda_3 > 0$. In particular, $\lim_{N \to \infty} \Lambda_2 = B/2$ where $B = 0.35$. This localized spectra differs largely from the spectra of nearest neighbour ring topologies given by Eq. (12), which covers the interval

$[2\mu - 1, 1]$ densely for large $N$. Although a more in-detail comparison between both setups is out of the scope of this paper, it is likely that transverse instabilitites in [19] only occur through $\Lambda_2$ and $\Lambda_3$ rather than several concurrently unstable eigenmodes. This might explain the disappearance of chaos for large networks in that setup.

These differences between non-local and local interactions in rings indicate that network topology and, specifically, their spectra, play an important role on the properties of the resulting dynamical states. Here, we restricted ourselves on simple structures, without an in-depth analyzis on how specific topological features affect the emergent behavior. Future work should analyze the effect of varying network density in both ring and Erdős-Rényi networks, or the impact of other topologies such as scale-free or small world.

On a different note, the extensive nature of the chaotic states and the patterns displayed in ring networks are an indication that this form of space-time chaos could correspond to a turbulent state. Moreover, the dependence of the growth rates on the structural eigenmodes depicted in Fig. 1(a) resembles that of the Benjamin-Feir instability in the complex Ginzburg-Landau equation[37]. Similar turbulent states have been studied in arrays of individual Kuramoto-Sakaguchi oscillators with non-local coupling[38–40]. Further analysis should thus address to what extent the properties of our setup for increasing $N$ match those of phase or amplitude turbulence in spatially extended systems[31].

Here we have studied the dynamics of the Kuramoto-Sakaguchi populations at the thermodynamic limit via the Ott-Antonsen equations. The global attractiveness of this low-dimensional manifold for $\Delta > 0$ has been recently proven[27], strengthening the validity of this approach to study networks of Kuramoto-Sakaguchi populations. Nonetheless, previous works have shown that (low-dimensional) chaotic dynamics unveiled by the Ott-Antonsen equations might display different properties in finite-size simulations[10]. A detailed comparison of simulations of the microscopic system (1) with finite $M$, and those of the Ott-Antonsen description Eq. (2), could provide valuable insights to understanding the convergence of Kuramoto-Sakaguchi ensembles to the low-dimensional manifold. Nonetheless, such study would require a large computational effort due to the large number of degrees of freedom involved.

Finally, although our study does not stem from any particular physical setup, the Kuramoto-Sakaguchi model successfully describes a wide variety of real-world phenomena, including power grids[41], circadian rhythms[42], and biofilms[43]. A particularly explored application is neural dynamics, where the Kuramoto-Sakaguchi model has been rigorously derived from spiking neuron models[44]. In this context, the mean-field description provided by the Ott-Antonsen equations offers a simplified neural mass model[7]. Thus, our analysis of the coupled system Eq. (2) provides a simple, yet grounded, framework to analyze whole brain dynamics where each brain region is represented by a Kuramoto-Sakaguchi population. In fact, the study of transverse instabilities in whole brain models is a powerful tool to unveil the multiscale dynamics of these systems, even when the single-node dynamics evolve according to generic neural mass models[45].

## Appendix A: Measures of collective activity

Here we describe the different quantitative measures employed to characterize the dynamics emerging from transverse instabilities in large networks of oscillator populations.

- To capture the macroscopic behavior of the system, we compute the mean Kuramoto order parameter

$$\mathcal{R}(t) := \frac{1}{N} \sum_{\sigma=1}^{N} R_\sigma(t)$$

and its instantaneous standard deviation on the network

$$\mathcal{S}(t) = \frac{1}{\sqrt{N}} \left\{ \sum_{\sigma=1}^{N} \left[ R_\sigma(t) - \mathcal{R}(t) \right]^2 \right\}^{\frac{1}{2}}.$$

If the network is at a heterogeneous state (in $R_\sigma$), then $\mathcal{S} > 0$.

- The chaotic activity of a system can be characterized by the corresponding Lyapunov exponents[46,47] which we denote by $\ell_\sigma$, where $\ell_1 \geq \ell_2 \geq \cdots \geq \ell_N$. We compute the Lyapunov exponents using the standard dynamical algorithm based on QR-decomposition[47,48]. In particular, simulations have been performed using the *DynamicalSystems.jl* Julia package[49] (see Appendix B for more details on numerical simulations).

- The fractal dimension of a chaotic attractor can be approximated using the Kaplan-Yorke formula[50], given by

$$\mathcal{D}_{\text{KY}} = j + \frac{\sum_{i=1}^{j} \ell_i}{|\ell_{j+1}|} \qquad \text{(A1)}$$

where $j$ is such that $\sum_{i=1}^{j} \ell_i \geq 0$ but $\sum_{i_1}^{j+1} \ell_i < 0$.

- Another measure of dynamical complexity is the Kolmogorov-Sinai dynamical entropy $h_{\text{KS}}$, which measures the growth rate of distinguishable trajectories in phase space[47,51]. Following Pesin's formula, $h_{\text{KS}}$ can be computed as the sum of all positive Lyapunov exponents

$$h_{\text{KS}} = \sum_{i=1}^{n} \ell_i. \qquad \text{(A2)}$$

where $n$ is such that $\ell_n \geq 0$ and $\ell_{n+1} < 0$.

## Appendix B: Numerical simulations and numerical continuation

The code used in this paper is openly available at `github.com/pclus/kuramoto-sakaguchi-network`. Simulations of the model and computation of Lyapunov exponents have been performed in Julia via the DynamicalSystems.jl package[49]. In particular we have employed the Runge-Kutta 4 algorithm with a fixed time step of $dt = 10^{-2}$.

Simulations of the system employed an initial transient evolution of 6000 time units. This is a conservative transient time set to achieve a good convergence near the bifurcations, but for most parameter values shorter transients provide the same results. After this transient, we simulate both, phase space and tangent space dynamics for the computation of the Lyapunov exponents. The tangent space is initially evolved for 200 time units, after which we start computing all the Lyapunov exponents for a total of 1000 time units. The QR decomposition for computation of the spectra is invoked at every time unit (i.e., $1/dt$ time steps).

Simulations of the the ring network have been initialized at the antiphase state with an additional small random perturbation. This prevents the system from stalling into a long chaotic transient in the region where the antiphase state is stable. For the random network, since no trivial antiphase state exists, simulations have been initialized at the homogeneous state with a random small perturbation.

Bifurcation diagrams of Fig. 2 have been partially obtained with auto-07p numerical continuation software[32]. In order to simplify the analysis, the 2-population model with the connectivity matrix (10), it has been rewritten as a three-dimensional system in real space by considering the polar representation of the Kuramoto complex parameters $Z_1 = R_1 e^{i\Phi_1}$ and $Z_2 = R_2 e^{i\Phi_2}$ and defining a new variable $\Theta = \Phi_1 - \Phi_2$. Then, Eq. (2) reads

$$\dot{R}_1 = -\Delta R_1$$
$$+ K\left(\frac{1-R_1^2}{2}\right)\left[\mu R_1 \cos(\alpha) + (1-\mu)R_2 \cos(\Theta - \alpha)\right]$$
$$\dot{R}_2 = -\Delta R_2$$
$$+ K\left(\frac{1-R_2^2}{2}\right)\left[\mu R_2 \cos(\alpha) + (1-\mu)R_1 \cos(\Theta + \alpha)\right]$$
$$\dot{\Theta} = K\left(\frac{1+R_1^2}{2R_1}\right)\left[\mu R_1 \sin(\alpha) - (1-\mu)R_2 \sin(\Theta - \alpha)\right]$$
$$- K\left(\frac{1+R_2^2}{2R_2}\right)\left[\mu R_2 \sin(\alpha) + (1-\mu)R_1 \sin(\Theta + \alpha)\right].$$

The auto-07p codes for the numerical continuation and a tutorial guide to obtain some of the bifurcations is openly available at `github.com/pclus/kuramoto-sakaguchi-network`.

## Appendix C: Parameter reduction

System (2) contains three parameters: $\Delta$, $K$, and $\alpha$. It is possible to rescale the system in order to reduce the parameter number to two. Some works[9,11,12] consider systems in which time is rescaled as $\tilde{t} = Kt$ so that the coupling strength $K$ can be removed from the equations or, equivalently, let it constant as $K = 1$. In this case Eq. (2) reads

$$\frac{dZ_\sigma}{d\tilde{t}} = -\tilde{\Delta}Z_\sigma + \frac{1}{2}\sum_{\kappa=1}^{N} c_{\sigma\kappa}\left(Z_\kappa e^{-i\alpha} - Z_\sigma^2 Z_\kappa^* e^{i\alpha}\right)$$

where $\tilde{\Delta} = \Delta/K$ and $K > 0$.

Another option is to rescale time as $\tilde{t} = \Delta t$, such that (2) reads

$$\frac{dZ_\sigma}{d\tilde{t}} = -Z_\sigma + \frac{\tilde{K}}{2}\sum_{\kappa=1}^{N} c_{\sigma\kappa}\left(Z_\kappa e^{-i\alpha} - Z_\sigma^2 Z_\kappa^* e^{i\alpha}\right).$$

with $\tilde{K} = K/\Delta$ and $\Delta > 0$. This would be equivalent to let $\Delta = 1$ fixed in the equations.

In this work we choose to not rescale any parameter in the system, so the analysis remains valid in all the extreme cases ($\Delta = 0$ and $K = 0$). Nonetheless, we are mostly interested in the heterogeneous case ($\Delta > 0$), thus we let $\Delta = 1$ without loss of generality. Therefore, in the 2-population model, the equivalence between the formulation of previous studies[9–12] and that given in Eq. (2) with $\Delta = 1$ is $D = 1/K$, $\mu = p$, $\nu = 1 - p$, and $A = \mu - \nu = 2p - 1$.

## Appendix D: Antiphase states in ring networks

Here we provide the stablity analysis of antiphase states in topologies provided by either Eq.(10) or Eq. (11) with an even number of populations $N$. This analysis is performed in close analogy to that performed in Section III. Antiphase states are solutions of Eq. (2) given by

$$Z_\sigma = \begin{cases} \hat{R}e^{i\hat{\Omega}t} & \text{if } \sigma \text{ is even} \\ \hat{R}e^{i(\hat{\Omega}t+\pi)} & \text{if } \sigma \text{ is odd.} \end{cases}$$

Inserting this expressions into Eq. (2) and using the corresponding expression of $c_{\sigma\kappa}$ we obtain that

$$\hat{R} = \sqrt{1 - \frac{2\Delta}{K(2\mu-1)\cos(\alpha)}} \quad \text{and} \qquad (D1)$$
$$\hat{\Omega} = \overline{\omega} - \tan(\alpha)[K(2\mu-1)\cos(\alpha) - \Delta].$$

By linearizing (2) around this solution we obtain

$$\dot{z}_\sigma = (-\Delta + i\overline{\omega} - K(2\mu-1)\hat{R}^2 e^{i\alpha})z_\sigma$$
$$+ \frac{K}{2}\sum_{\kappa=1}^{M} c_{\sigma\kappa}(z_\kappa e^{-i\alpha} - \hat{R}^2 z_\kappa^* e^{i\alpha}).$$

By choosing $\overline{\omega} = \tan(\alpha)[K(2\mu-1)\cos(\alpha) - \Delta]$ and replacing the expression of $\hat{R}$ from Eq.(D1) we obtain

$$\dot{z}_\sigma = \hat{A}z_\sigma + \hat{B}\sum_{\kappa=1}^{N} c_{\sigma\kappa}z_\kappa$$

where

$$\hat{A} = \begin{pmatrix} \Delta - K\cos(\alpha)(2\mu - 1) & -\Delta\tan(\alpha) \\ \Delta\tan(\alpha) & \Delta - K\cos(\alpha)(2\mu - 1) \end{pmatrix}$$

and

$$\hat{B} = \begin{pmatrix} \frac{\Delta}{2\mu-1} & \frac{\Delta}{2\mu-1}\tan(\alpha) \\ -K\sin(\alpha) + \frac{\Delta}{2\mu-1}\tan(\alpha) & K\cos(\alpha) - \frac{\Delta}{2\mu-1} \end{pmatrix}.$$

Analogously to the stability of the homogeneous states in Section III, we apply the MSF formalism based on decomposing a perturbation on the basis of the eigenvectors of the connectivity matrix $C$. As a result we obtain that the stability of the antiphase state is provided by the eigenvalues of the $N$ $2 \times 2$ matrices:

$$\hat{M}_k = \hat{A} + \Lambda_k\hat{B} \quad \text{for} \quad k = 1, \ldots, N;$$

where $\Lambda_k$ are provided by Eq. (12). The explicit expression of the system eigenvalues read:

$$\hat{\lambda}_k^{(\pm)} = \Delta + K\cos(\alpha)\left(\frac{\Lambda_k}{2} + 1 - 2\mu\right)$$
$$\pm \left\{ \frac{K^2\Lambda_k^2\cos^2(\alpha)}{4} \right.$$
$$+ \frac{K\Lambda_k\Delta\cos(\alpha)}{2\mu-1}\left[\tan^2(\alpha)(2\mu - 1 - \Lambda_k) - \Lambda_k\right]$$
$$+ \left. \frac{\Delta^2}{(2\mu-1)^2}\left[(\Lambda_k^2 - (2\mu-1)^2)\tan^2(\alpha) + \Lambda_k^2)\right]\right\}^{1/2}.$$
$$\text{(D2)}$$

From this expression we shall highlight several aspects:

- As in the homogeneous state, the antiphase state is a periodic solution in a co-rotating frame. Therefore at least one of the eigenvalues has to be 0. This corresponds to $\Lambda_N = 2\mu - 1$, as the associated eigenvector indicates perturbations acting opposite on each node consecutively, i.e., from Eq. (13):

$$\Psi_j^{(N)} = \begin{cases} \frac{1}{\sqrt{N}} & \text{if } j \text{ is odd,} \\ \frac{-1}{\sqrt{N}} & \text{if } j \text{ is even.} \end{cases}$$

- Taking into account the previous point, for $N = 2$ the stability of the antiphase solution is controlled by the eigenvalue associated to $k = 1$. Substituting thus $\Lambda_1 = 1$ in Eq. (D2) and solving for $\lambda_1^{(\pm)} = 0$ we obtain the bifurcations from the antiphase state in the 2-population model. This eigenvalue can be zero through a pair of complex conjugates or a single real eigenvalue, defining thus the subcritical Hopf (H-) and the pitchfork (PF'-) bifurcations displayed in Fig. 2.

- For $N > 2$ other eigenvalues rather than $\Lambda_1$ can lead to instabilities of the antiphase state. This is the case of Fig. 4, in which the left branch of the instability is always given by $\Lambda_1$, but the right branch corresponds to other modes depending on $N$.

**Appendix E: Transverse instabilities of the incoherent state**

Here study transverse instabilities of the incoherent homogeneous state $Z_\sigma = 0 =: Z^{(0)}$ for $\sigma = 1, \ldots, N$. Our aim is to show that transverse instabilities do not arise when this state is stable, i.e., when $0 < K\cos(\alpha) < 2\Delta$. Without loss of generality, we impose $\overline{\omega} = 0$. Then, by linearizing Eq. (2) around the incoherent solution $Z^{(0)}$ we obtain

$$\dot{z}_\sigma = -\Delta\omega z_\sigma + \frac{K}{2}\sum_{\kappa=1}^{M} c_{\sigma\kappa}z_\kappa e^{-i\alpha} = A^{(0)}z_\sigma + B^{(0)}\sum_{\kappa=1}^{N} c_{\sigma\kappa}z_\kappa,$$

where

$$A^{(0)} = \begin{pmatrix} -\Delta & 0 \\ 0 & -\Delta \end{pmatrix}$$

and

$$B^{(0)} = \frac{K}{2}\begin{pmatrix} \cos(\alpha) & \sin(\alpha) \\ -\sin(\alpha) & \cos(\alpha) \end{pmatrix}.$$

Following again the Master Stability formalism presented in Section III, the stability of this solution is controlled by the eigenvalues $\lambda_k^{(\pm)}$ of the matrices

$$M_k^{(0)} = A^{(0)} + \Lambda_k B^{(0)} \quad \text{for} \quad k = 1, \ldots, N;$$

Now, instead of finding a general expression for the eigenvalues it is enough to see that

$$\text{Tr}(M_k^{(0)}) = \lambda_k^{(+)} + \lambda_k^{(-)} = \Lambda_k K\cos(\alpha) - 2\Delta.$$

The incoherent solution $Z^{(0)}$ is stable within the homogeneous manifold Eq. (3) if and only if $K\cos(\alpha) < 2\Delta$. In this case, since $0 < \Lambda_k < 0$ and $\Delta > 0$, we have that $\text{Tr}(M_k^{(0)}) < 0$. Therefore, transverse instabilities of the incoherent state may emerge only if it is already unstable to homogeneous perturbations.

[1] Y. Kuramoto and D. Battogtokh, "Coexistence of coherence and incoherence in nonlocally coupled phase oscillators," Nonlinear Phenom. Complex Syst. **5**, 380 (2002).

[2] D. M. Abrams and S. H. Strogatz, "Chimera States for Coupled Oscillators," Physical Review Letters **93**, 174102 (2004).

[3] F. Parastesh, S. Jafari, H. Azarnoush, Z. Shahriari, Z. Wang, S. Boccaletti, and M. Perc, "Chimeras," Physics Reports **898**, 1–114 (2021).

[4] S. W. Haugland, "The changing notion of chimera states, a critical review," Journal of Physics: Complexity **2**, 032001 (2021).

[5] H. Sakaguchi and Y. Kuramoto, "A Soluble Active Rotater Model Showing Phase Transitions via Mutual Entertainment," Progress of Theoretical Physics **76**, 576–581 (1986), https://academic.oup.com/ptp/article-pdf/76/3/576/5302137/76-3-576.pdf.

[6] E. Ott and T. M. Antonsen, "Low dimensional behavior of large systems of globally coupled oscillators," Chaos: An Interdisciplinary Journal of Nonlinear Science **18**, 037113 (2008).

[7] C. Bick, M. Goodfellow, C. R. Laing, and E. A. Martens, "Understanding the dynamics of biological and neural oscillator networks through exact mean-field reductions: A review," The Journal of Mathematical Neuroscience **10**, 9 (2020).

[8] See also the Watanabe-Strogatz theory[52], which provides a complete description for the homogeneous case. For a comprehensive general theory that includes and relates Watanabe-Strogatz and Ott-Antonsen frameworks see Ref. [27].

[9] C. R. Laing, "Chimera states in heterogeneous networks," Chaos: An Interdisciplinary Journal of Nonlinear Science 19, 013113 (2009).

[10] C. R. Laing, "Disorder-induced dynamics in a pair of coupled heterogeneous phase oscillator networks," Chaos: An Interdisciplinary Journal of Nonlinear Science 22, 043104 (2012).

[11] T. Kotwal, X. Jiang, and D. M. Abrams, "Connecting the Kuramoto Model and the Chimera State," Physical Review Letters 119, 264101 (2017).

[12] S. Guo, M. Yang, W. Han, and J. Yang, "Dynamics in two interacting subpopulations of nonidentical phase oscillators," Physical Review E 103, 052208 (2021).

[13] D. M. Abrams, R. Mirollo, S. H. Strogatz, and D. A. Wiley, "Solvable Model for Chimera States of Coupled Oscillators," Physical Review Letters 101, 084103 (2008).

[14] For studies of non-identical populations (i.e., ensembles governed by different parameter values) see [53–55].

[15] E. A. Martens, "Chimeras in a network of three oscillator populations with varying network topology," Chaos: An Interdisciplinary Journal of Nonlinear Science 20, 043122 (2010).

[16] E. A. Martens, "Bistable chimera attractors on a triangular network of oscillator populations," Physical Review E 82, 016216 (2010).

[17] S. Lee and K. Krischer, "Chaotic chimera attractors in a triangular network of identical oscillators," Physical Review E 107, 054205 (2023).

[18] S. Lee and K. Krischer, "Heteroclinic switching between chimeras in a ring of six oscillator populations," Chaos: An Interdisciplinary Journal of Nonlinear Science 33, 063120 (2023).

[19] C. R. Laing, "Chimeras on a ring of oscillator populations," Chaos: An Interdisciplinary Journal of Nonlinear Science 33, 013121 (2023).

[20] L. M. Pecora and T. L. Carroll, "Master stability functions for synchronized coupled systems," Phys. Rev. Lett. 80, 2109–2112 (1998).

[21] D. Ruelle, "Large volume limit of the distribution of characteristic exponents in turbulence," Communications in Mathematical Physics 87, 287–302 (1982).

[22] H.-w. Xi, R. Toral, J. D. Gunton, and M. I. Tribelsky, "Extensive chaos in the nikolaevskii model," Phys. Rev. E 62, R17–R20 (2000).

[23] M. R. Paul, M. I. Einarsson, P. F. Fischer, and M. C. Cross, "Extensive chaos in rayleigh-bénard convection," Phys. Rev. E 75, 045203 (2007).

[24] M. Monteforte and F. Wolf, "Dynamical entropy production in spiking neuron networks in the balanced state," Phys. Rev. Lett. 105, 268104 (2010).

[25] A. Palmigiano, R. Engelken, and F. Wolf, "Boosting of neural circuit chaos at the onset of collective oscillations," (2022), 10.1101/2022.08.28.505598.

[26] K. A. Takeuchi, H. Chaté, F. Ginelli, A. Politi, and A. Torcini, "Extensive and subextensive chaos in globally coupled dynamical systems," Phys. Rev. Lett. 107, 124101 (2011).

[27] R. Cestnik and A. Pikovsky, "Exact finite-dimensional reduction for a population of noisy oscillators and its link to Ott–Antonsen and Watanabe–Strogatz theories," Chaos: An Interdisciplinary Journal of Nonlinear Science 32, 113126 (2022).

[28] See Refs. [56–58] for introductory reviews on the MSF formalism. Although most studies on the MSF rely on diffusive coupling or variations of it via a Laplacian matrix (see, e.g., [59]), the method is applicable to any setup having a homogeneous solution (see, e.g., [45]).

[29] J. Wilkinson, The Algebraic Eigenvalue Problem, Monographs on numerical analysis (Clarendon Press, 1967).

[30] The homogeneous synchronized solution emerges only for $\Delta - K\cos(\alpha)/2 < 0$, which leads to $\Delta + K\cos(\alpha)\left(\frac{\Lambda}{2} - 1\right) < 0$ in Eq. (9) (since $\Delta \geq 0$ and $-1 \leq \Lambda \leq 1$). Therefore, eigenvalues with positive real part in Eq. (9) always correspond to real eigenvalues. Complex conjugate eigenvalues might exist, but they correspond to stable directions.

[31] Y. Kuramoto, Chemical Oscillations, Waves and Turbulence (Springer, Berlin, 1984).

[32] E. J. Doedel, A. R. Champneys, F. Dercole, T. F. Fairgrieve, Y. A. Kuznetsov, B. Oldeman, R. Paffenroth, B. Sandstede, X. Wang, and C. Zhang, "Auto-07p: Continuation and bifurcation software for ordinary differential equations," (2007).

[33] For $\alpha = 1.2$ we did not find the chaotic state unveiled in [10], but it can be attained, for instance, at $(K, \mu, \alpha, \Delta) = (20, 0.9, 1.25, 1)$.

[34] J. M. Lopez and F. Marques, "Dynamics of Three-Tori in a Periodically Forced Navier-Stokes Flow," Physical Review Letters 85, 972–975 (2000).

[35] D. Pazó and V. Pérez-Muñuzuri, "Onset of wave fronts in a discrete bistable medium," Physical Review E 64, 065203 (2001).

[36] C. R. Laing, "The dynamics of chimera states in heterogeneous Kuramoto networks," Physica D: Nonlinear Phenomena 238, 1569–1588 (2009).

[37] T. B. Benjamin and J. E. Feir, "The disintegration of wave trains on deep water part 1. theory," Journal of Fluid Mechanics 27, 417–430 (1967).

[38] M. Wolfrum, S. V. Gurevich, and O. E. Omel'chenko, "Turbulence in the Ott–Antonsen equation for arrays of coupled phase oscillators," Nonlinearity 29, 257–270 (2016).

[39] M. Bolotov, L. Smirnov, G. Osipov, and A. Pikovsky, "Simple and complex chimera states in a nonlinearly coupled oscillatory medium," Chaos: An Interdisciplinary Journal of Nonlinear Science 28, 045101 (2018).

[40] M. I. Bolotov, L. A. Smirnov, E. S. Bubnova, G. V. Osipov, and A. S. Pikovsky, "Spatiotemporal Regimes in the Kuramoto–Battogtokh System of Nonidentical Oscillators," Journal of Experimental and Theoretical Physics 132, 127–147 (2021).

[41] G. Filatrella, A. H. Nielsen, and N. F. Pedersen, "Analysis of a power grid using a Kuramoto-like model," The European Physical Journal B 61, 485–491 (2008).

[42] S. H. Strogatz, "Human sleep and circadian rhythms: A simple model based on two coupled oscillators," Journal of Mathematical Biology 25, 327–347 (1987).

[43] J. Liu, R. Martinez-Corral, A. Prindle, D. yeon D. Lee, J. Larkin, M. Gabalda-Sagarra, J. Garcia-Ojalvo, and G. M. Süel, "Coupling between distant biofilms and emergence of nutrient time-sharing," Science 356, 638–642 (2017), https://www.science.org/doi/pdf/10.1126/science.aah4204.

[44] P. Clusella, B. Pietras, and E. Montbrió, "Kuramoto model for populations of quadratic integrate-and-fire neurons with chemical and electrical coupling," Chaos: An Interdisciplinary Journal of Nonlinear Science 32, 013105 (2022).

[45] P. Clusella, G. Deco, M. L. Kringelbach, G. Ruffini, and J. Garcia-Ojalvo, "Complex spatiotemporal oscillations emerge from transverse instabilities in large-scale brain networks," PLOS Computational Biology 19, e1010781 (2023).

[46] A. Politi, "Lyapunov exponent," Scholarpedia 8, 2722 (2013), revision #137286.

[47] A. Pikovsky and A. Politi, Lyapunov Exponents: A Tool to Explore Complex Dynamics (Cambridge University Press, Cambridge, 2016).

[48] G. Benettin, L. Galgani, A. Giorgilli, and J.-M. Strelcyn, "Lyapunov Characteristic Exponents for smooth dynamical systems and for hamiltonian systems; A method for computing all of them. Part 2: Numerical application," Meccanica 15, 21–30 (1980).

[49] G. Datseris, "Dynamicalsystems.jl: A julia software library for chaos and nonlinear dynamics," Journal of Open Source Software 3, 598 (2018).

[50] J. L. Kaplan and J. A. Yorke, "Chaotic behavior of multidimensional difference equations," in Functional Differential Equations and Approximation of Fixed Points, edited by H.-O. Peitgen and H.-O. Walther (Springer Berlin Heidelberg, Berlin, Heidelberg, 1979) pp. 204–227.

[51] Y. Sinai, "Kolmogorov-Sinai entropy," Scholarpedia 4, 2034 (2009).

[52] X.-J. Wang and G. Buzsáki, "Gamma Oscillation by Synaptic Inhibition in a Hippocampal Interneuronal Network Model," The Journal of Neuroscience 16, 6402–6413 (1996).

[53] E. Montbrió, J. Kurths, and B. Blasius, "Synchronization of two interacting populations of oscillators," Phys. Rev. E 70, 056125 (2004).

[54] E. A. Martens, C. Bick, and M. J. Panaggio, "Chimera states in two populations with heterogeneous phase-lag," Chaos: An Interdisciplinary Journal of Nonlinear Science 26, 094819 (2016).

[55] C.-U. Choe, J.-S. Ri, and R.-S. Kim, "Incoherent chimera and glassy states in coupled oscillators with frustrated interactions," Phys. Rev. E 94, 032205 (2016).

[56] A. Arenas, A. Díaz-Guilera, J. Kurths, Y. Moreno, and C. Zhou, "Synchronization in complex networks," Physics Reports 469, 93–153 (2008).

[57] M. Porter and J. Gleeson, Dynamical Systems on Networks: A Tutorial, Frontiers in Applied Dynamical Systems: Reviews and Tutorials (Springer International Publishing, 2016).

[58] P. Ashwin, S. Coombes, and R. Nicks, "Mathematical frameworks for oscillatory network dynamics in neuroscience," The Journal of Mathematical Neuroscience 6, 2 (2016).

[59]H. Nakao, "Complex Ginzburg-Landau equation on networks and its non-uniform dynamics," The European Physical Journal Special Topics **223**, 2411–2421 (2014).